Chinese Chemical Letters 32 (2021) 2899–2903

Contents lists available at ScienceDirect

Chinese Chemical Letters

journal homepage: www.elsevier.com/locate/cclet

Communication

Surface-tuned two-dimension MXene scaffold for highly reversible zinc metal anode

Xiaoyu Liu[a,1], Yongzheng Fang[b,1], Pengcheng Liang[a,1], Jiahao Xu[c], Bo Xing[c,*], Kai Zhu[b,*], Yuyu Liu[a], Jiujun Zhang[a], Jin Yi[a,*]

[a] Department of Chemistry & Institute for Sustainable Energy, Shanghai University, Shanghai 200444, China
[b] Key Laboratory of Superlight Materials and Surface Technology (Ministry of Education), College of Material Science and Chemical Engineering, Harbin Engineering University, Harbin 150001, China
[c] College of Mechanical and Electrical Engineering, Jiaxing University, Jiaxing 314001, China

ARTICLE INFO

Article history:
Received 7 February 2021
Received in revised form 23 February 2021
Accepted 23 February 2021
Available online 26 February 2021

Keywords:
MXene
Surface-tuned engineering
Nucleation
Zn anodes
Zn ion batteries

ABSTRACT

Zinc metal has aroused increasing interest as anode material of Zn-based batteries for their energy storage application. However, the uneven Zn stripping/plating processes induce severe dendrite growth, leading to low Coulombic efficiency and safety hazards. Herein, a surface-tuned two-dimensional (2D) MXene $Ti_3C_2T_x$ scaffold as a robust skeleton is developed to facilitate the uniform Zn stripping/plating. The $Ti_3C_2T_x$ with high electrical conductivity and unique structure provides fast ionic-transport paths, promising even Zn^{2+} stripping/plating processes. With suppressed Zn dendrite growth and uniform nucleation, the proposed 2D $Ti_3C_2T_x$ scaffold for Zn metal anode delivers a low voltage hysteresis of 63 mV and long lifespan over 280 h. This surface-tuned engineering strategy demonstrates the potential application of Zn anode with MXene skeleton for next-generation Zn-based batteries.

Lithium-ion batteries (LIBs) have been widely utilized in energy storage due to their high specific capacity (3860 mAh/g) and the low standard reduction potential (−3.004 V *vs.* standard hydrogen electrode (SHE)) [1–5]. However, Li dendrite growth and flammability of organic electrolyte could trigger potential safety issues [6,7]. Besides, the limited lithium resources result in the growing economic cost and environmental challenge. Compared to LIBs, aqueous Zn-based batteries (AZBs) are considered as promising alternatives owing to their decent safety and cost-effectiveness [8–11]. By far, various aqueous Zn-based batteries have been developed, including Zn-air batteries, Zn-V_2O_5 batteries and Zn-MnO_2 batteries [12–14]. Unfortunately, the challenging issues associated with Zn anodes, such as Zn dendrite growth, Zn corrosion, hydrogen evolution reaction and shape change, hinder their applications in large-scale energy storage devices [15,16].

Zn dendrite growth is usually caused by the uneven current distribution, concentration polarization and non-uniform nucleation sites. Generally, the initial nucleation is localized and inhomogeneous, and the subsequent ions tend to rapidly deposit on the protrusions of the anode to minimize surface energy [17]. During the subsequent cycles, the continuous growth of Zn dendrite tips gives rise to irreversible capacity loss, and could eventually lead to catastrophic safety hazards. Therefore, the design concept of controllable Zn nucleation through forming a uniform current distribution and nucleation site for Zn^{2+} is of great significance to novel Zn anodes in AZBs. To address the above problems, different strategies have been developed, such as surface modification [18,19], structure design [20,21], and electrolyte optimization [22–25]. The surface modification and electrolyte optimization could effectively manipulate the interface between Zn electrode and electrolyte, leading to the improved lifespan of the battery. By contrast, structure design mainly focuses on improving the uniformity of Zn ion deposition. Scientists have reported numerous strategies of structure design, including three-dimensional (3D) Zn framework and Zn plated hierarchical electrode, which could provide a high surface area and alleviate the local current density, resulting in homogeneous Zn ion nucleation and stable striping/plating behavior. Particularly, the Zn plated electrode is favorable to wide application in AZBs due to its simple fabrication process and stable structure. For the

* Corresponding authors.
E-mail addresses: xingbo@mail.zjxu.edu.cn (B. Xing), kzhu@hrbeu.edu.cn (K. Zhu), jin.yi@shu.edu.cn (J. Yi).
[1] These authors contributed equally to this work.

https://doi.org/10.1016/j.cclet.2021.02.055
1001-8417/

construction of Zn plated electrode, exploring a capable substrate with high conductivity and abundant Zn deposition sites is the key to suppress Zn dendrite growth.

MXene has attracted tremendous attention in energy storage and conversion community because of its lamellar structure, good metallic electrical conductivity, fast ion transport and superior mechanical/chemical stabilities [26–32]. The general formula of MXene is $M_{n+1}X_n$, where M symbolizes early transition metal, and X donates a carbon, nitrogen atom, or carbon-nitrogen diatoms. The selective etching methods involving fluoride-containing acidic solutions have been widely used to prepare MXenes, which are prone to be terminated by the functional groups of −O, −OH, −F and −Cl [33]. Even though the investigations of MXene as a substrate for Li and Na anodes have been widely reported, few efforts have been posed on developing novel Zn metal anodes with MXene for AZBs [34]. Because of strong electronegativity of F functional groups, the MXene with rich F functional groups would result in the uneven current distribution and non-uniform nucleation sites for Zn. Meanwhile, the F-rich MXene usually delivers unfavorable electrical conductivity [35,36]. Therefore, the investigation of the relationship between F functional groups in MXene and the Zn plating/stripping behavior is highly inspiring for developing Zn anode with high-performance.

Herein, a two-dimensional (2D) $Ti_3C_2T_x$ MXene scaffold with low-content of F functional group (LF-$Ti_3C_2T_x$) as the robust skeleton is proposed for Zn anode with high electrochemical performance (Fig. 1). Unlike the uneven deposition of Zn ions and vertical growth of Zn dendrites on commercial Ti-based current collector (Ti mesh), Zn ions are uniformly plated on Ti-based MXene LF-$Ti_3C_2T_x$, leading to horizontal growth of Zn on the surface of LF-$Ti_3C_2T_x$. The lamellar structure and high electrical conductivity of 2D $Ti_3C_2T_x$ with low content of F functional group scaffold offer fast ionic-transport paths, even current distribution, and uniform nucleation sites for Zn^{2+}. Consequently, a low voltage hysteresis of 63 mV and a long lifespan over 280 h are obtained for Zn anode with 2D MXene. This work demonstrates the potential application of MXene as a capable substrate for the Zn metal anode.

Few-layer $Ti_3C_2T_x$ MXene with lamellar structure has been prepared *via* solution-based etching method to remove Al atom-layer from Ti_3AlC_2, as evidenced in the results of scanning electron microscopy (SEM) and transmission electron microscopy (TEM) (Figs. 2a–c). The obtained $Ti_3C_2T_x$ nanosheets display an ultrathin structure (~three layers). The formation of $Ti_3C_2T_x$ MXene can be further confirmed by the X-ray powder diffraction (XRD) patterns. In Fig. 2d, the typical (002) peak of MXene is observed while the standard (104) peak in Ti_3AlC_2 disappears after etching, indicating the complete removal of Al and the successful preparation of $Ti_3C_2T_x$.

The electrochemical performance of the pristine $Ti_3C_2T_x$ as the current collector for Zn anode has been investigated, as displayed in Fig. S1 (Supporting information). It can be seen that the charging/discharging voltage profiles are irregular and the corresponding Coulombic efficiency is unfavorable, probably attributed to a large amount of F functional groups with strong electronegativity in MXene scaffold which would disturb the migration of Zn^{2+} and the subsequent Zn deposition. In order to decrease the content of F functional group, and the sample of LF-$Ti_3C_2T_x$ MXene was prepared through the heat treatment at the Ar atmosphere. XPS tests were carried out to determine the chemical composition on the surface of $Ti_3C_2T_x$ MXene and LF-$Ti_3C_2T_x$ MXene, and the obtained spectra are shown in Figs. 2e and f, indicating the sharp drop of F content within the MXene scaffold after the heat treatment. Therefore, it is expected that the Zn anode based on the LF-$Ti_3C_2T_x$ MXene scaffold can exhibit superior electrochemical performance. Fortunately, from the results of, it can be found that the favorable 2D laminated morphologies of MXene remain unchanged after the heat treatment process, demonstrated by SEM and TEM images of the LF-$Ti_3C_2T_x$ MXene sample (Fig. S2 in Supporting information).

Furthermore, the XRD pattern (Fig. 2d) of LF-$Ti_3C_2T_x$ MXene indicates that the lamellar structure of $Ti_3C_2T_x$ MXene keeps stable after heat treatment at the Ar atmosphere and the absence of TiO_2 peak implies a low oxidation degree of MXene. In addition, the (002) peak shifted to the right after heat treatment, which could be attributed to the disappearance of the interlayer water [37]. In order to further investigate the chemical composition and the corresponding chemical bonding state in LF-$Ti_3C_2T_x$ MXene, XPS tests were carried out, and the full spectrum analysis is shown in Fig. 2e. In contrast to $Ti_3C_2T_x$, interestingly, the peak intensity of the -F group in LF-$Ti_3C_2T_x$ obviously decreases, indicating that numerous -F terminals on $Ti_3C_2T_x$ are sheared after heat treatment, which is beneficial for higher electrode conductivity (Fig. 2f) [38]. Meanwhile, it can be seen that the main elements of LF-$Ti_3C_2T_x$ are C, Ti and O. As for the high-resolution XPS spectrum of C 1s (Fig. S3 in Supporting information), four peaks at binding energies of 287.2, 286.1, 284.6 and 282.7 eV can be deconvoluted, which are assigned to C=O, C—O, C—C and C—Ti, respectively. For O 1s, the peaks at 533.7, 531.8 and 530.3 eV are assigned to C—OH, Ti—OH and Ti—O–Ti, respectively. The peaks at 464.4 and 459.1 eV correspond to the Ti $2p_{1/2}$ and Ti $2p_{3/2}$ of Ti species in Ti—O, while the peaks at 455.8 eV are assigned to Ti $2p_{3/2}$ of Ti—C [26]. The above results are similar to the typical properties of reported Ti_3C_2 MXene, which also indicate that the heat treatment at the Ar atmosphere has a negligible effect on the other functional groups of MXene.

With the aim to study the plating/stripping processes of Zn, the CV measurements were employed at a scanning rate of 0.1 mV/s and a voltage window of −0.3~1.5 V (*vs.* Zn/Zn^{2+}). As shown in Fig. 3a, the reduction peak (at −0.17 V) and the oxidation peak (at 0.17 V) corresponding to the plating/stripping behavior of Zn can be observed, which indicates high reversibility of Zn on LF-$Ti_3C_2T_x$. In addition, during the plating/stripping process, the oxidation peak decreases gradually with the decrease of the corresponding reduction peak current. It is worth noting that a reduction peak occurring at the potential of 0.7 V during the initial cycle can be observed in the inset of the CV curve, which will be further investigated in the following section. To demonstrate the advantage of Ti-based MXene LF-$Ti_3C_2T_x$ as a capable substrate for Zn plating, a commercial Ti mesh substrate is chosen as a comparison. Fig. 3b shows the voltage-capacity curves of the first plating process of Zn on different current collectors in a half-cell, in which the Ti mesh or LF-$Ti_3C_2T_x$ is the cathode and bare Zn foil is the anode. During the first discharge, Zn^{2+} is reduced to metallic zinc and plated on the current collector. As an important parameter to evaluate the performance of the current collector, the nucleation overpotential is referred to as the voltage difference between the lowest voltage and equilibrium potential during the plating

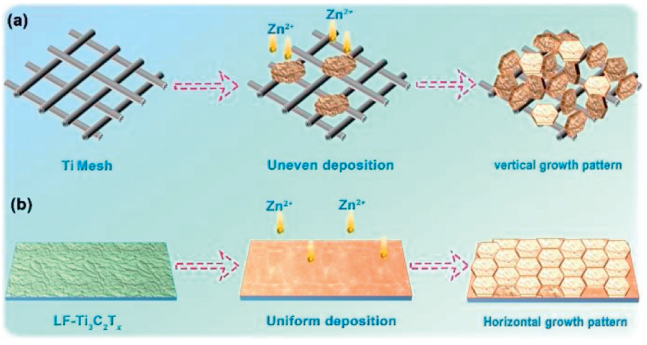

Fig. 1. The schematic of Zn plating different hosts.

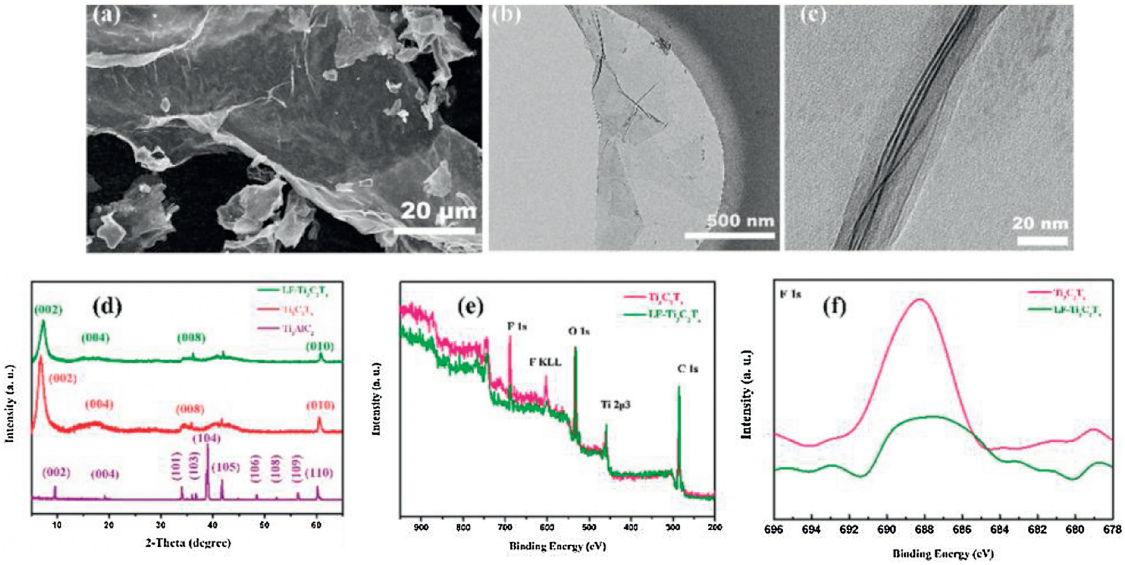

Fig. 2. (a) SEM, (b) TEM and (c) HR-TEM images of $Ti_3C_2T_x$ MXene. (d) XRD and (e, f) XPS of $Ti_3C_2T_x$ MXene and LF-$Ti_3C_2T_x$ MXene.

process. It can be observed that the nucleation overpotentials are 65.4 and 32 mV on Ti and LF-$Ti_3C_2T_x$ current collectors, respectively. The lower nucleation overpotential of LF-$Ti_3C_2T_x$ demonstrates the smaller nucleation barrier and more uniform nucleation behavior. Moreover, it is worth noting that an obvious discharge platform around 0.7 V is observed for LF-$Ti_3C_2T_x$, corresponding to the CV curve in Fig. 3a well. Combined with the results of XPS characterization, the discharge platform would be derived from the irreversible reactions between Zn^{2+} and oxygen-containing functional groups in the LF-$Ti_3C_2T_x$ host, which is common in alkaline metal battery systems [33]. The voltage polarization and Coulomb efficiency of Zn anodes are considered as important factors to evaluate the electrochemical performance of current collectors. Figs. 3c and d display the voltage-capacity curves of Zn plating/stripping processes on Ti and LF-$Ti_3C_2T_x$, respectively. The average voltage polarization of the Ti current collector is 60.3 mV. The Coulombic efficiency of the initial cycle is lower than that of the subsequent cycle, indicating that the plated metal zinc on Ti is not completely stripped and returned to the Zn sheet. Furthermore, with the charge/discharge cycle going on, the voltage curve begins to be unstable with a slight voltage drop only since the 30th cycle. Severe voltage changes occur at the 35th cycle with the Coulomb efficiency of 43.3%, indicating uneven plating/stripping behaviors and fast formation of dendritic Zn. When LF-$Ti_3C_2T_x$ is used as a current collector, favorable results can be obtained. The average voltage polarization of 53 mV is achieved, which is lower than the voltage polarization of the Ti current collector. However, the Coulombic efficiency of the initial cycle is lower than that of Ti current collector, which would be ascribed to the irreversible reactions taking place between the oxygen-containing functional groups of LF-$Ti_3C_2T_x$ and Zn^{2+}. With the cycle increasing, the Zn plating/stripping processes on LF-$Ti_3C_2T_x$ current collector show high Coulombic efficiency and stable plating/stripping curves over 50 cycles, suggesting high reversibility and uniform Zn growth. With the increase of current density, the nucleation potentials of Zn plating increase on Ti and LF-$Ti_3C_2T_x$ current collectors, which indicates that the current density has a certain influence on the plating behavior of Zn. In addition, it can be clearly observed that the nucleation overpotential of Zn plating on LF-$Ti_3C_2T_x$ is lower than that plating on Ti, which can be found in Fig. 3e. These results indicate that LF-$Ti_3C_2T_x$ can reduce the nucleation potential of zinc deposition, promoting uniform deposition, and inhibiting the Zn dendrite growth. In order to evaluate the cyclic stability of Zn@LF-$Ti_3C_2T_x$ as Zn anode for AZB, the symmetrical cells were tested at different current densities and capacities. Before the tests, 10 mAh/cm^2 Zn metal was deposited in current collectors by electrodeposition method at 10 mA/cm^2, named Zn@Ti and Zn@LF-$Ti_3C_2T_x$. Then, the symmetrical batteries were assembled using the two identical prepared Zn anodes. As shown in Fig. 3f, during the initial state, the Zn@Ti//Zn@Ti cell displays smaller polarization than that with Zn@LF-$Ti_3C_2T_x$ due to the 3D structure of Ti mesh. However, the Zn@Ti//Zn@Ti cell shows a large voltage change after 35 h at 5 mA/cm^2, which would be derived from the formation of ZnO layer on the surface of Zn with the increased internal resistance and unstable voltage curves [15]. On the contrary, the Zn@LF-$Ti_3C_2T_x$//Zn@LF-$Ti_3C_2T_x$ cell delivers a stable cycle for 280 h with an average polarization voltage of 63 mV. The voltage platform is relatively stable with slight fluctuation, indicating uniform plating/striping behaviors induced by the LF-$Ti_3C_2T_x$ scaffold.

The above results demonstrate that the LF-$Ti_3C_2T_x$ current collector can improve the reversibility of zinc plating/stripping processes, significantly reduce the local current density and voltage polarization. Meanwhile, the Zn@LF-$Ti_3C_2T_x$ composite exhibits good cyclic stability.

In order to investigate the morphologies of Zn deposition on different current collectors, the SEM characterizations were carried out. Compared with the pristine Ti current collector, the uneven Zn morphology has been observed after 50 cycles on the Ti current collector with the Zn capacity of 1 mAh/cm^2, as displayed in Figs. 4a and b. With Zn capacity increased to 2.5 mAh/cm^2, the vertically growing Zn dendrites are observed without any flat surface, which demonstrates that the Zn dendrite growth would be more serious with the increase of Zn deposition (Fig. 4c). Compared to the bare LF-$Ti_3C_2T_x$ current collector (Fig. 4d), the Zn on LF-$Ti_3C_2T_x$ presents a flat and smooth morphology under 1 mAh/cm^2 (Fig. 4e). Even with a high capacity of 2.5 mAh/cm^2 (Fig. 4f), the Zn deposition is still flat and presents a horizontal growth pattern without any dendrites. According to the previous studies, $Ti_3C_2T_x$ can induce metal ions to be arranged according to the spatial structure of MXene [39,40]. Therefore, the lateral growth of Zn may be related to the induced deposition effect of MXene. Considering the above results and discussions, it can be found that the LF-$Ti_3C_2T_x$ can guide uniform Zn deposition and limited Zn dendrite growth, thereby leading to

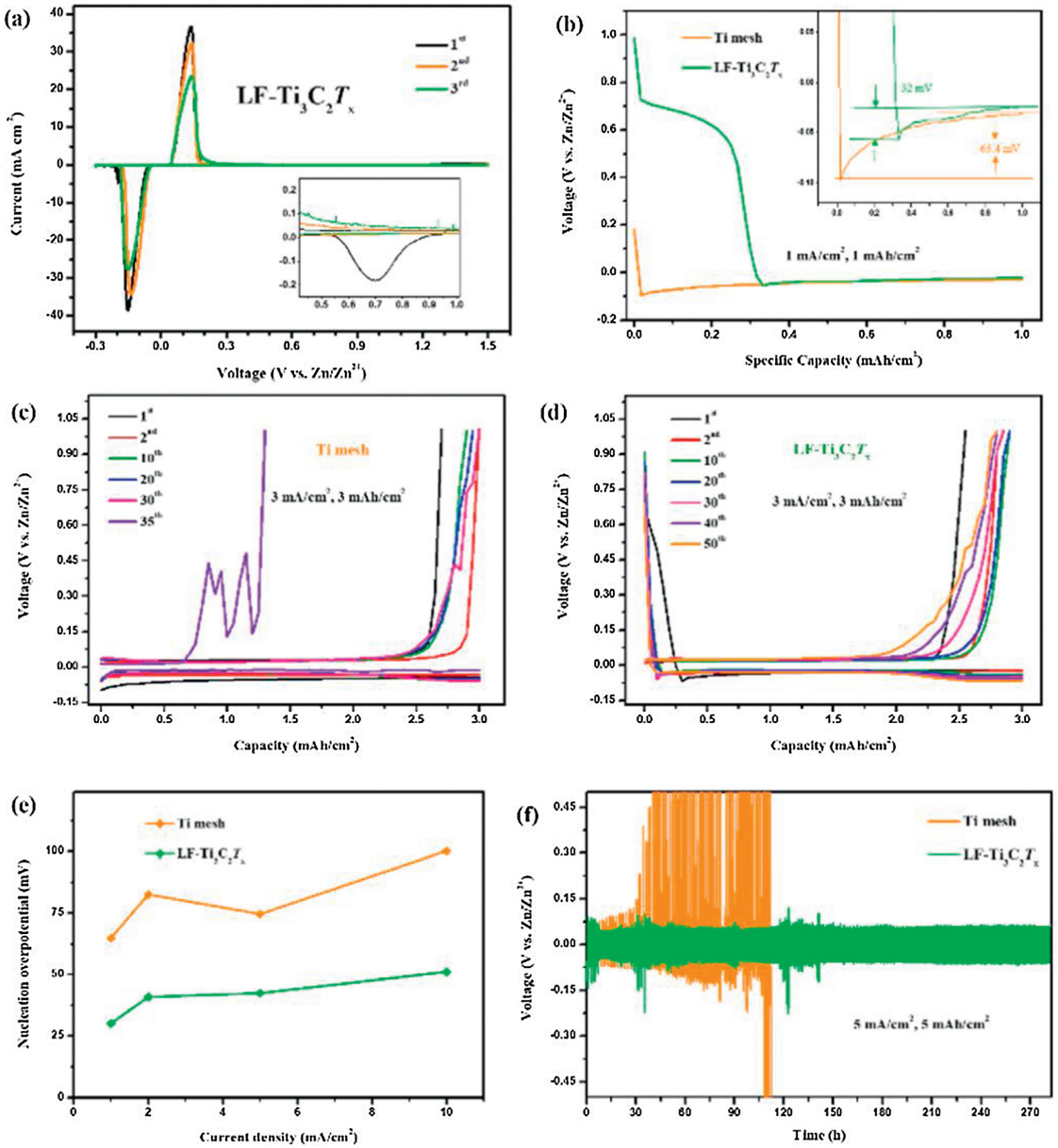

Fig. 3. (a) CV curves of Zn//LF-$Ti_3C_2T_x$ half-cell at a scan rate of 0.1 mV/s. (b) Voltage-time curves during Zn nucleation at 1 mA/cm^2 on Ti mesh and LF-$Ti_3C_2T_x$ electrodes. Inset: an enlargement voltage-time curves. Voltage profiles of (c) Zn//Ti and (d) Zn//LF-$Ti_3C_2T_x$ half-cells at a current density of 3 mA/cm^2 with a capacity of 3 mAh/cm^2. (e) Nucleation overpotential of Zn deposited on Ti mesh and LF-$Ti_3C_2T_x$ scaffold at current densities of 1, 2, 5 and 10 mA/cm^2 with deposition capacity of 1, 2, 5 and 10 mAh/cm^2, respectively. (f) Voltage profiles of symmetric cells of Zn@Ti and Zn@LF-$Ti_3C_2T_x$ at 5 mA/cm^2 with a capacity of 5 mAh/cm^2.

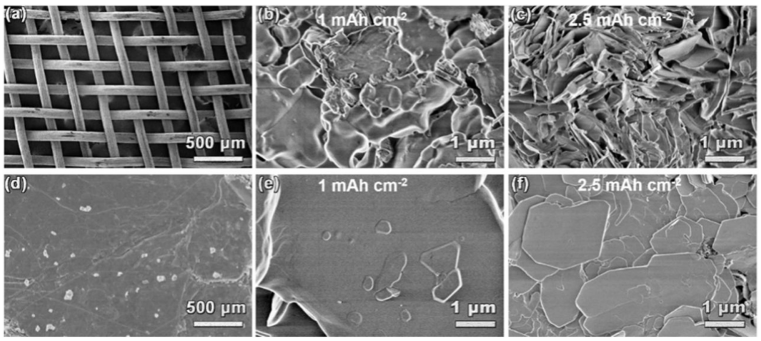

Fig. 4. SEM images of Zn plating on (a – c) Ti mesh and (d – f) LF-$Ti_3C_2T_x$ before and after 50 cycles at 5 mA/cm^2 with various capacities.

stable plating/stripping processes and long cycling performance. These favorable electrochemical behaviors can not only be attributed to the excellent conductivity of the less-F MXene, but also to the induced deposition effect of MXene.

In summary, a surface-tuned two-dimension (2D) MXene scaffold with low-content of F functional group as the robust skeleton is developed under high temperature at the atmosphere of Ar. The uneven Zn stripping/plating processes for Zn^{2+} have been achieved when employing the LF-$Ti_3C_2T_x$ as a current collector. The low voltage hysteresis of 63 mV and long lifespan over 280 h are obtained. The proposed surface-tuned engineering would facilitate the application of MXene as the robust skeleton for next-generation batteries.

Declaration of competing interest

The authors report no declarations of interest.

Acknowledgments

The authors are grateful for the partial financial support from the National Natural Science Foundation of China (Nos. 21805182, 22075171), Shanghai Pujiang Program (No. 18PJ1403800).

Appendix A. Supplementary data

Supplementary material related to this article can be found, in the online version, at doi:https://doi.org/10.1016/j.cclet.2021.02.055.

References

[1] J.Y. Luo, W.J. Cui, P. He, et al., Nat. Chem. 2 (2010) 760–765.
[2] H. Yu, Y.G. So, Y. Ren, et al., J. Am. Chem. Soc. 140 (2018) 15279–15289.
[3] J. Yi, X. Li, S. Hu, et al., J. Power Sources 196 (2011) 6670–6675.
[4] Q. Zhang, H. Chen, L. Luo, et al., Energy Environ. Sci. 11 (2018) 669–681.
[5] Z. Zheng, H.H. Wu, H. Liu, et al., ACS Nano 14 (2020) 9545–9561.
[6] X.B. Cheng, T.Z. Hou, R. Zhang, et al., Adv. Mater. 28 (2016) 2888–2895.
[7] J. Yi, C. Wang, Y. Xia, Electrochem. Comm. 33 (2013) 115–118.
[8] M. Song, H. Tan, D. Chao, et al., Adv. Funct. Mater. 28 (2018) 1802564.
[9] N. Zhang, F. Cheng, Y. Liu, et al., J. Am. Chem. Soc. 138 (2016) 12894–12901.
[10] P. Liang, J. Yi, X. Liu, et al., Adv. Funct. Mater. 30 (2020) 1908528.
[11] K. Wu, J. Huang, J. Yi, et al., Adv. Energy Mater. 10 (2020) 1903977.
[12] X. Liu, J. Yi, K. Wu, et al., Nanotechnology 31 (2020) 122001.
[13] F. Cui, J. Zhao, D. Zhang, et al., Chem. Eng. J. 390 (2020) 124118.
[14] X. Yu, F. Hu, F. Cui, et al., Dalton Trans. 49 (2020) 1048–1055.
[15] J. Yi, P. Liang, X. Liu, et al., Energy Environ. Sci. 11 (2018) 3075–3095.
[16] W. Du, E.H. Ang, Y. Yang, et al., Energy Environ. Sci. 13 (2020) 3330–3360.
[17] Z. Zhao, J. Zhao, Z. Hu, et al., Energy Environ. Sci. 12 (2019) 1938–1949.
[18] K. Zhao, C. Wang, Y. Yu, et al., Adv. Mater. Interfaces 5 (2018) 1800848.
[19] L. Kang, M. Cui, F. Jiang, et al., Adv. Energy Mater. 8 (2018) 1801090.
[20] Z. Kang, C. Wu, L. Dong, et al., ACS Sustainable Chem. Eng. 7 (2019) 3364–3371.
[21] Z. Wang, J. Huang, Z. Guo, et al., Joule 3 (2019) 1289–1300.
[22] L. Chladil, O. Čech, J. Smejkal, et al., J. Energy Storage 21 (2019) 295–300.
[23] A. Naveed, H. Yang, J. Yang, et al., Angew. Chem. Int. Ed. 58 (2019) 2760–2764.
[24] W. Xu, K. Zhao, W. Huo, et al., Nano Energy 62 (2019) 275–281.
[25] Z. Liu, T. Cui, G. Pulletikurthi, et al., Angew. Chem. Int. Ed. 55 (2016) 2889–2893.
[26] M. Naguib, M. Kurtoglu, V. Presser, et al., Adv. Mater. 23 (2011) 4248–4253.
[27] M. Lu, H. Li, W. Han, et al., J. Energy Chem. 31 (2019) 148–153.
[28] H. Tang, W. Li, L. Pan, et al., Adv. Funct. Mater. 29 (2019) 1901907.
[29] X. Zhang, R. Lv, A. Wang, et al., Angew. Chem. Int. Ed. 130 (2018) 15248–15253.
[30] M.Q. Zhao, X. Xie, C.E. Ren, et al., Adv Mater. 29 (2017) 1702410.
[31] M. Naguib, M. Kurtoglu, V. Presser, et al., Adv. Mater. 23 (2011) 4207-4207.
[32] Z.L. Hu, X.X. Kuai, J.T. Chen, et al., ChemSusChem 13 (2020) 1485–1490.
[33] Y.Z. Fang, R. Fang, K. Zhu, et al., Adv. Funct. Mater. 30 (2020) 2005663.
[34] Y. Tian, Y. An, C. Wei, et al., ACS Nano 13 (2019) 11676–11685.
[35] P. Liu, W. Ding, J. Liu, et al., J. Alloys. Compd. 829 (2020) 154634.
[36] L. Huang, T. Li, Q. Liu, et al., Electrochem. Comm. 104 (2019) 106472.
[37] Tao Minmin, Zhaojin, et al., ACS Nano 12 (2018) 3578–3586.
[38] J.L. Hart, K. Hantanasirisakul, A.C. Lang, et al., Nat. Commun. 10 (2019) 522.
[39] Y. Fang, R. Lian, H. Li, et al., ACS Nano 14 (2020) 8744–8753.
[40] Y. Fang, Y. Zhang, K. Zhu, et al., ACS Nano 13 (2019) 14319–14328.